

Numerical Estimation of Underwater Radiated Noise of a Marine Propeller in Non-cavitating Regime



Abhishek Kumar Tewari, Vijit Misra and R. Vijayakumar

Abstract The underwater radiated noise levels (RNLs) emanating from surface and underwater marine platforms are becoming a topic of significant concern for all the nations in view of the global requirement to minimise the increasing adverse impact on marine life and maintain ecological balance in the so-called silent ocean environment. The studies have reported an increase in low-frequency ambient sea noise by an average rate of about 1/2 dB per year [Ross in *IEEE J Ocean Eng* 30(2):257–261, 2005 1] which is attributable to the growing fleet of ships. Marine propeller noise in both non-cavitating and cavitating regimes is an important component of the overall underwater radiated noise of a marine platform in addition to the machinery and flow noise. Merchant ships generally operate at low speeds, and hence, propeller noise in non-cavitating regime is an important area of concern. For military applications, design of low-noise propellers dictates the ships' survivability and operational performance. Hence, design and development of low-noise propulsion systems and, in particular, low-noise propellers is a relevant topic of current focus which is in line with the global need of the hour to design eco-friendly ships. In this respect, the main scope of this study is to numerically calculate the propeller noise in the non-cavitating regime for the uniform flow (no wake condition). Flow around the propeller is solved with a commercial CFD software STAR-CCM+, while hydro-acoustic analysis is performed using Ffowcs Williams–Hawkings (FWH) equation. The numerical closure was achieved using $k-\epsilon$ Reynolds-averaged Navier–Stokes (RANS) model. The predicted hydrodynamic performance curves and radiated noise levels have been validated from the published experimental and numerical results.

Keywords Underwater radiated noise · Sound pressure level
Hydrodynamic performance · Blade passage frequency · Cavitation

A. K. Tewari (✉) · V. Misra · R. Vijayakumar
Indian Institute of Technology Madras, Chennai 600036, Tamil Nadu, India
e-mail: abhishek.navyguy@gmail.com

© Springer Nature Singapore Pte Ltd. 2019
K. Murali et al. (eds.), *Proceedings of the Fourth International Conference in Ocean Engineering (ICOE2018)*, Lecture Notes in Civil Engineering 22,
https://doi.org/10.1007/978-981-13-3119-0_10

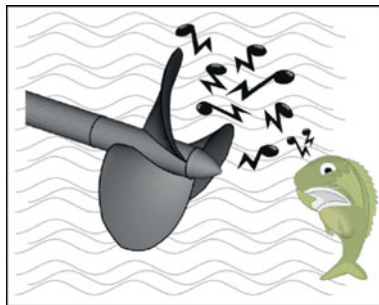
1 Introduction

The underwater radiated noise generated by a surface or underwater marine platform has gained significant global concern in recent times in view of the growing impetus on the analysis and minimisation of harmful effects of the increase in the ‘ambient noise’ on the marine ecosystem. The ocean is rightly called the ‘silent world’ where there is no room for any foreign noise/disturbance. Over the last few decades, the studies have reported an increase in low-frequency ambient sea noise by an average rate of about 1/2 dB per year which is attributable to the growing fleet of ships both commercial and military vessels. When we consider sources of ambient noise in deep water, the distance ship traffic is a dominant source of noise at frequencies around 100 Hz, and high ship-traffic activity is dominant source of noise in the frequencies from 50 to 500 Hz [2]. In case of military vessels, the radiated noise also effects the detectability, operability as well as survivability of the vessel.

Ships’ underwater radiated noise comprises the machinery noise, propeller noise and hydrodynamic flow noise. The propeller noise consists of both cavitating and non-cavitating noises. The merchant ships generally operate at low speeds (less than cavitation inception speed), and hence, the propeller noise in the non-cavitating region also becomes an important concern. Also, for deeply submerged vehicles, where cavitation does not occur, the non-cavitating noise becomes an important factor. The design intent is aimed at delaying the inception of propeller cavitation to speed greater than the normal operating/cruising speeds. Hence, it becomes important to study and quantify the propeller non-cavitating noise and identify and implement design steps to delay cavitation inception (Fig. 1).

Marine propellers operate in a highly three-dimensional turbulent wake field behind a ship, which makes it very complicated and difficult to resolve the flow-field variables. In order to perform the hydro-acoustic analysis and predict the noise generated by the propellers, it is first required to carry out the hydrodynamic analysis of the flow and estimate the flow parameters like velocities and pressure. This can be done either by experimental as well as numerical approaches. Several attempts have been made in the past by many researchers to estimate the propeller performance experimentally. Experimental works carried out by Amini and Steen [3], Liu et al.

Fig. 1 DTMB 4119 propeller model *Source* Mousavi et al. [15]



[4] and Elghorab et al. [5] are relevant in this regard. But conducting the experiments requires complicated set-ups, and these are very expensive both in terms of time and cost. An alternative to this approach is conducting numerical simulations which have also been found very useful in undertaking these studies. These numerical methods have used both inviscid and viscous flow methods.

The noise which is detected in a fluid can be generated due to two reasons, namely due to the vibrations of the structure and due to the hydrodynamic fluid fluctuations. In the present study, only the noise generated by fluid fluctuations has been estimated.

Generally, to estimate the propeller-generated noise empirical, semi-empirical and Bernoulli-based methods have been used. But the generation of a method by aero-acousticians Ffowcs Williams–Hawkings (FWH) for calculation of noise generated by an arbitrary moving body in a fluid is considered as a novel development in this direction.

Seol et al. [6] investigated the non-cavitating propeller noise in non-uniform flow using potential-based panel method coupled with acoustic analogy (FWH equation) and boundary element method (BEM). Seol et al. [7] extended their work to estimation of propeller noise in the cavitating regime. The flow field was analysed with potential-based panel method, and the time-dependent pressure and sheet cavity volume data were used as the input for FWH formulation to predict the far-field acoustics.

In 2003, Salvatore and Ianniello [8] undertook numerical prediction of the acoustic pressure field induced by cavitating marine propellers using boundary integral formulations. A hydrodynamic model for transient sheet cavitation on propellers in non-uniform inviscid flow was coupled with a hydro-acoustic model based on the FWH equation. The study brought out splitting of the noise signature into thickness and loading term contributions. The predictions using the FWH equation were found to be close agreement with those obtained using Bernoulli equation model. Several attempts have been made in the recent years by many researchers to predict the non-cavitating propeller noise in uniform as well as non-uniform flow using various CFD codes coupled with either FWH equations or in-house built noise prediction codes.

In the present study, the underwater RNL of a DTMB 4119 model propeller has been predicted by a 3D numerical simulation of the flow around the propeller operating in the non-cavitating regime for the uniform flow (no wake) condition. For the near field, the RANS equations have been used for modelling the flow, and the k - ϵ model has been used to simulate the turbulence. For the far-field acoustic, the FWH model has been applied. FWH steady and FWH-on-the-fly models have been used in the steady and transient analyses, respectively. Analysis of the radiated sound pressure level with respect to distance from the propeller has been carried out, and the results obtained have been discussed. The open water hydrodynamic characteristics obtained using numerical simulation have been validated with the published experimental results. The SPL predicted for the design advance coefficient (J) of 0.833 has been compared with the available published numerical results. Further, the SPLs have been predicted for different advance coefficients, and the results obtained have been discussed.

2 Governing Equations

While performing the hydrodynamic analysis of fluid flow, the flow-field variables can be predicted by solution of the two basic equations, namely the continuity (Eq. 1) and momentum equations (Eq. 2).

$$\frac{\partial \rho}{\partial t} + \frac{\partial}{\partial x_i}(\rho u_i) = 0 \quad (1)$$

$$\frac{\partial}{\partial t}(\rho u_i) + \frac{\partial}{\partial x_j}(\rho u_i u_j) = \frac{\partial}{\partial x_j} \tau_{ij} - \frac{\partial p}{\partial x_i} + \rho g_i - \rho \bar{u}_i \bar{u}_j \quad (2)$$

where u_i is the velocity components of the fluid, ρ is the density, p is the pressure, τ is the shear stress tensor, g is the acceleration due to gravity and $\bar{u}_i \bar{u}_j$ is the Reynolds stress tensor. Equations (1) and (2) are coupled and should be solved simultaneously in an iterative manner.

The estimation of the distribution of Reynolds stress throughout the flow field has been the subject of numerous investigations. In this study, the k- ϵ model has been used to simulate the turbulence. This model has been used in many recent hydro-acoustic estimations like the studies undertaken by Ghassemi et al. in 2016 and 2017.

The first and most recognised work in the field of acoustic waves has been done by Lighthill (1952). The two basic governing equations of the continuity and momentum are employed to obtain overall sound production relationship by writing the continuity equation as follows:

$$\frac{D\rho}{Dt} + \text{div}(\rho \bar{u}) = \frac{\partial \rho}{\partial t} + \frac{\partial}{\partial x_i}(\rho u_i) = q \quad (3)$$

where q is the mass production rate per unit volume. The momentum equation is expressed as:

$$\frac{\partial}{\partial t}(\rho u_i) + \frac{\partial}{\partial x_j}(\rho u_i u_j) = -\frac{\partial p}{\partial x_i} - \frac{\rho g \partial \tau}{\partial x_i} + f_i \quad (4)$$

where f_i represents the body forces. From Eqs. (3) and (4), Eq. (5) is obtained as follows:

$$\frac{\partial^2 \rho}{\partial t^2} + c_0^2 \nabla^2 p = \partial^2(T_{ij})/\partial x_i \partial x_j \quad (5)$$

where c_0 is the speed of sound and T_{ij} is the Lighthill stress tensor. It is expressed as

$$T_{ij} = \rho u_i u_j + \delta_{ij}(p - \rho c_0^2) + \tau_{ij} \quad (6)$$

The first term on the RHS of Eq. (6) is the turbulence velocity fluctuations (Reynolds stresses), the second term is due to change in pressure and density, and the third term is due to the shear stress tensor.

A generalisation of Lighthill’s theory to include aerodynamic surfaces in motion proposed by Ffowcs Williams–Hawkings (1969) has provided the basis for a significant amount of analysis of the noise produced by rotating blades, including helicopter rotors, propeller blades and fans. The FWH theory includes surface source terms in addition to the quadrupole-like sources introduced by Caridi (2007). The surface sources are generally referred to as thickness or monopole sources and loading or dipole sources. This equation is presented as follows (FWH 1969):

$$\frac{\partial^2 p'}{c_0^2 \partial t^2} - \nabla^2 p' = \frac{\partial^2}{\partial x_i \partial x_j} [T_{ij} H(f)] - \frac{\partial}{\partial x_i} ([P_{ij} n_j + \rho u_i (u_n - v_n)] \delta(f)) + \frac{\partial}{\partial t} ([\rho_0 v_n + \rho (u_n - v_n)] \delta(f)) \tag{7}$$

The terms at the RHS of Eq. (7) are named quadrupole, dipole and monopole sources, respectively, p' is the source pressure level at the far field ($p' = p - p_0$), c_0 is the far-field sound speed and T_{ij} is the Lighthill stress tensor defined in Eq. (6). Also, f is a function defined based on surface reference system where setting $f = 0$ introduces a surface that embeds the external flow effect ($f > 0$), and $H(f)$ and $\delta(f)$ are Heaviside and Dirac delta functions, respectively.

There are various ways to evaluate the FWH equation. Farassat proposed time-domain formulation that can predict arbitrary-shaped object in motion without the numerical differentiation of the observer time. The formulation of Farassat is very convenient in embodying the time-domain analysis of FWH equation. In the Farassat formulation, the pressure field is defined as:

$$P'(\vec{x}, t) = P'_T(\vec{x}, t) + P'_L(\vec{x}, t) \tag{8}$$

where P' is the acoustic pressure, P'_T and P'_L describe the acoustic pressure field resulting from thickness and loading, corresponding to the monopole and the dipole sources. In the present analysis, quadrupole noise has been neglected since the speed of rotation of the propeller is much less than the speed of sound in water.

By solving this equation, pressure variation and sound pressure level (SPL) measured in dB are calculated as follows:

$$\text{SPL} = 20 \log_{10} \left(\frac{P_{\text{rms}}}{P_{\text{ref}}} \right) \tag{9}$$

where P_{rms} is the root-mean-square sound pressure expressed in P_a and P_{ref} is the reference pressure of 1 μPa .

3 Numerical Modelling

The propeller model selected to undertake this analysis is the three-bladed DTMB4119 propeller which was originally designed by Denny. The data of this propeller was distributed to various research institutes by the ITTC propulsion committee for undertaking hydrodynamic research. Eight organisations including BEC France, HSVA Germany, HMRI Korea, SRI Japan, DERA UK, VTT Finland, University of Iowa USA and CSSRC China had conducted RANS calculations on the DTMB P4119 propeller and discussed the results during the workshop on Propulsion Committee held during 22nd ITTC [9]. Numerical modelling of the propeller and associated geometric parts has been undertaken using the commercial design software Rhino 3D. The solution of the flow around the propeller has been done using the commercial CFD code STAR-CCM+; the hydro-acoustic analysis has been performed using the in-built aero-acoustic analysis utility of STAR-CCM+. The details of the numerical modelling including propeller geometry, computational domain, boundary conditions and meshing have been discussed in subsequent paragraphs.

3.1 Geometry

The geometry data of DTMB4119 propellers has been obtained from Brizzolara et al. [10], and the foil geometry has been obtained from the Report of the Propulsion Committee [11]. The details of this propeller are indicated in Table 1, and the front view of the propeller modelled for the present study using Rhino 3D software is shown in Fig. 2. The origin is located at the centre of the propeller, and the coordinate system has been selected such that positive x -axis is towards the upstream direction of the propeller, positive z -axis is upwards and positive y -axis is inwards into the plane.

Fig. 2 DTMB 4119 propeller model

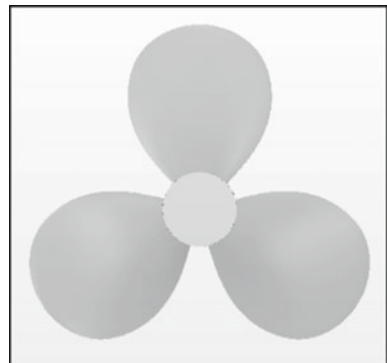


Table 1 DTMB4119 propeller geometry data

(a) Propeller geometry data						
Prop	4119					
r/R	c/D	rk/D	sk [°]	P/D	t_{max}/c	f_{max}/c
0.20	0.3200	0.00	0.00	1.1050	0.2055	0.0143
0.30	0.3635	0.00	0.00	1.1022	0.1553	0.0232
0.40	0.4048	0.00	0.00	1.0983	0.1180	0.0230
0.50	0.4392	0.00	0.00	1.0932	0.0902	0.0218
0.60	0.4610	0.00	0.00	1.0879	0.0696	0.0207
0.70	0.4622	0.00	0.00	1.0839	0.0542	0.0200
0.80	0.4347	0.00	0.00	1.0811	0.0421	0.0197
0.90	0.3613	0.00	0.0000	1.0785	0.0332	0.0182
0.95	0.2775	0.00	0.00	1.0770	0.0323	0.0163
0.98	0.2045	0.00	0.00	1.0761	0.0321	0.0145
1.00	0.0800	0.00	0.00	1.0750	0.0316	0.0118

(b) Hydrofoil geometry data			
Foil geometry at conventional stations NACA 66(Mod) and $a = 0.8$ camber			
Station	Thickness ordinate	Camber ordinate	Camber slope
x	Y_T/t	Y_C/f	$\frac{dY_C/f}{dx}$
0	0	0	–
0.005	0.0665	0.0423	7.149
0.0075	0.0812	0.0595	6.617
0.0125	0.1044	0.0907	5.944
0.025	0.1466	0.1586	5.023
0.05	0.2066	0.2712	4.083
0.075	0.2525	0.3657	3.515
0.1	0.2907	0.4482	3.100
0.15	0.3521	0.5869	2.488
0.2	0.4000	0.6993	2.023
0.25	0.4363	0.7905	1.635
0.3	0.4637	0.8635	1.292
0.35	0.4832	0.9202	0.933
0.4	0.4952	0.9615	0.678
0.45	0.5	0.9881	0.385
0.5	0.4962	1.0	0.091
0.55	0.4846	0.9971	–0.211
0.6	0.4653	0.9786	–0.532
0.65	0.4383	0.9434	–0.885
0.7	0.4035	0.8892	–1.295

(continued)

Table 1 (continued)

(b) Hydrofoil geometry data			
Foil geometry at conventional stations NACA 66(Mod) and $a = 0.8$ camber			
Station	Thickness ordinate	Camber ordinate	Camber slope
0.75	0.3612	0.8121	-1.813
0.8	0.3110	0.7027	-2.712
0.85	0.2532	0.5425	-3.523
0.9	0.1877	0.3586	-3.768
0.95	0.1143	0.1713	-3.668
0.975	0.0748	0.0823	-3.441
1.0	0.0333	0	-3.003
(c) Model scale propeller details			
Type	DTMB4119		
Diameter (D)	305 mm		
Hub diameter (d)	60 mm		
No of blades (Z)	3		
Pitch ratio (P/D) at 0.7R	1.084		
RPS	10		
Design J	0.833		
Design V_A	2.54 m/s		
Pitch	0°		
Skew	0°		
NACA section shape	66 (Mod)		
NACA meanline	0.8		

3.2 Domain

The computational domain along with all the parts and boundary conditions is shown in Fig. 3. It consists of an outer cylinder of length $18D$ and diameter $10D$ surrounding the propeller. A small cylinder of length $0.385D$ and diameter $1.1D$ is placed around the propeller. This cylinder represents the interface and is used to simulate the propeller rotation. The outer cylinder along with the shaft and the inner cylinder/interface constitutes the stationary part, and the propeller along with the hub and the inner cylinder/interface constitutes the rotating part. The open water condition has been applied to the inlet. The sizing of the domain is in accordance with the ITTC recommended guidelines for undertaking ship self-propulsion studies using CFD [12].

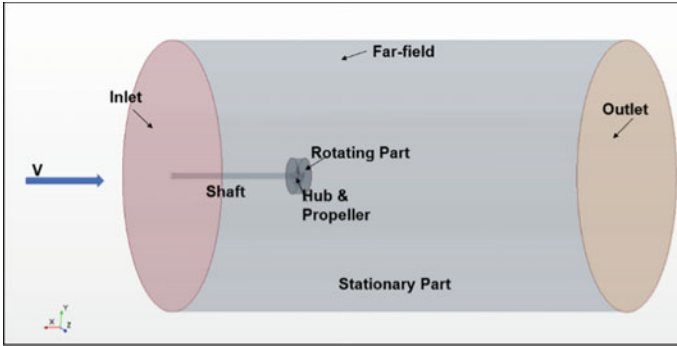


Fig. 3 Computational domain

Table 2 Boundary conditions

Region: stationary region	
Inlet	Velocity inlet
Outlet	Pressure outlet
Far field	Walls with slip condition

3.3 Boundary Conditions

The boundary conditions followed in the analysis are indicated in Table 2.

3.4 Meshing

An unstructured hybrid mesh was applied for grid generation. The meshing models selected for the present analysis are surface remesher, trimmer and prism layer mesher. Triangular cells have been used for meshing the blades and hub surfaces. Coarse grid has been used on the far field, and a finer grid has been used for near wall on the propeller blades, tip, interface to accurately capture the flow phenomenon in this region. The prism layer has been disabled from the inlet, outlet and far-field regions. All this have been done to reduce the computational time. A cylindrical volumetric mesh refinement has been applied around the rotating region to further refine the mesh in the region of interest. Three different base sizes, 30, 40 and 50 mm, has been used for the convergence study. The results of this have been discussed later in this paper. A cross section of the volume mesh on a vertical plane passing through the origin is shown in Fig. 4.

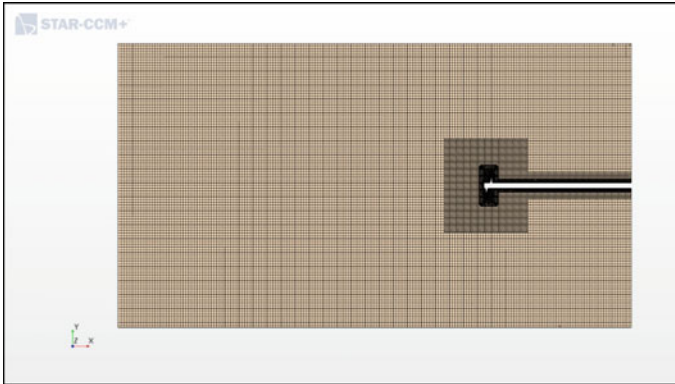


Fig. 4 Meshed computational domain

3.5 Acoustic Analysis

The hydro-acoustic analysis has been carried out by suitable modification of the aero-acoustic utility of the CFD code. SPL has been estimated using the FWH equations for both steady and transient states. For the steady-state analysis, the propeller rotation has been modelled using moving reference frame (MRF) method. Moving reference frames (MRFs) are reference frames that can rotate and translate with respect to the laboratory reference frame. MRF models in STAR-CCM+ assume that the angular velocity of the body is constant and the mesh is rigid. For the transient analysis, the propeller rotation has been modelled using moving reference frame (MRF) as well as sliding mesh methods. In the sliding mesh method, the region containing the propeller geometry is meshed as a separate region, and a purely rotational motion is applied to the entire propeller mesh. This results in a transient calculation, which provides time-accurate results [13]. A quantitative comparison with respect to the two methods has been brought out. The position of the six FWH receivers (A1, A2, A3, B1, B2 and B3) with respect to the propeller is shown in Fig. 5.

4 Hydrodynamic Analysis and Findings

4.1 Convergence Analysis

The K_T , $10K_Q$ and η_O convergence analyses were examined for three base sizes, i.e. 20, 30 and 50 mm, leading to 6,710,447, 2,180,027 and 564,806 cells, respectively. A comparison of the K_T , $10K_Q$ and η_O values obtained for the design J of 0.833 for the three base sizes along with error analysis is shown in Table 3. From the analysis,

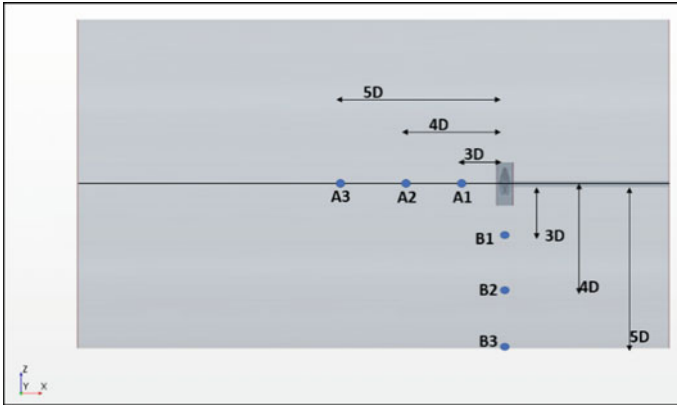


Fig. 5 Location of the FWH receivers

Table 3 Convergence analysis

Base size (mm)	$10K_Q$ -expt	K_T -expt	η_O -expt	$10K_Q$ -pred	K_T -pred	η_O -pred	$10K_Q$ -error	K_T -error	η_O -error
20	0.28	0.145	0.69	0.248	0.126	0.673	11.26	13.01	2.50
30	0.28	0.145	0.69	0.251	0.127	0.670	10.45	12.56	2.88
50	0.28	0.145	0.69	0.255	0.128	0.664	9.11	12.04	3.75

it was found that base size of 30 mm results in the least error, and hence, this base size was chosen for further analysis.

4.2 Open Water Characteristics

The open water characteristics of DTMB4119 model were estimated as a function of the advance coefficients for J values of 0.2, 0.4, 0.6, 0.8 and 1 using the steady-state analysis. From the convergence analysis, base size of 30 mm was selected for this simulation. Simulation for each value of J was executed for 550 iterations which took a physical time of about 10 h to complete the analysis and obtain the desired residuals. The processor used is Intel® Xenon® CPU E5-1620 v4 @ 3.50 GHz, and the installed memory is 16 GB. The variation of J was achieved by varying the value of advance velocity (V_A) and keeping the propeller rotation rate constant.

The predicted open water characteristics were compared with the experimental results of Jessup et al. (1989) which have been obtained from the calculation results for the 22nd ITTC Propulsor Committee Workshop on Propeller RANS/PANEL Methods [14]. The comparison shows matching with an error of 2.88% in the open water efficiency at the design J of 0.833 (Fig. 6).

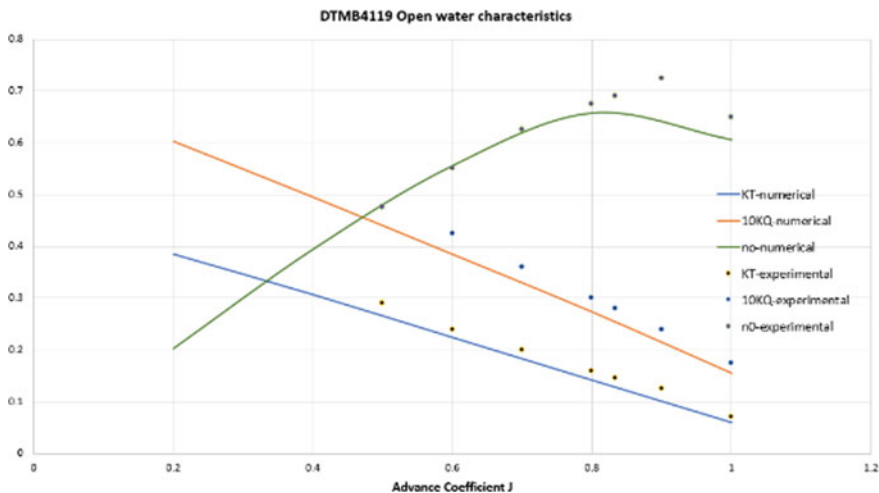


Fig. 6 Comparison of numerical and experimental results of the open water characteristics of DTMB4119 model propeller

5 Acoustic Analysis and Findings

The hydro-acoustic analysis has been performed by suitable modification of the in-built aero-acoustics utility of the CFD software. The density and the speed of sound in the medium, i.e. water, were changed to 1000 kg/m^3 and 1500 m/s , respectively. The propeller surface has been modelled as the impermeable FWH surface. The contribution from the hub has been neglected. Six receiver locations have been used in the analysis.

5.1 Steady-State Analysis

Initially steady-state analysis was carried out for $J = 0.833$, and the time series of acoustic pressures was obtained. Fourier transformation of this time series was undertaken to obtain the frequency distribution of the sound pressure levels. The pressure time history and frequency distribution of SPL are shown in Fig. 7.

Figure 7a shows the pressure-time history predicted for $J = 0.833$ at the three receivers A1, A2 and A3 placed in line with the hub towards the downstream of the propeller. It can be seen that the acoustic pressure decreases from receiver A1 to A3 since the distance from the acoustic source/propeller increases in this direction. The SPL versus frequency distribution at receiver A1, A2 and A3 has been obtained using fast Fourier transformation (FFT) of the pressure-time histories predicted at these locations and shown in Fig. 7b. Two characteristic peaks/tonals are visible at 10 and 20 Hz in each of these SPL distributions. Pattern similar to Fig. 7a is also seen

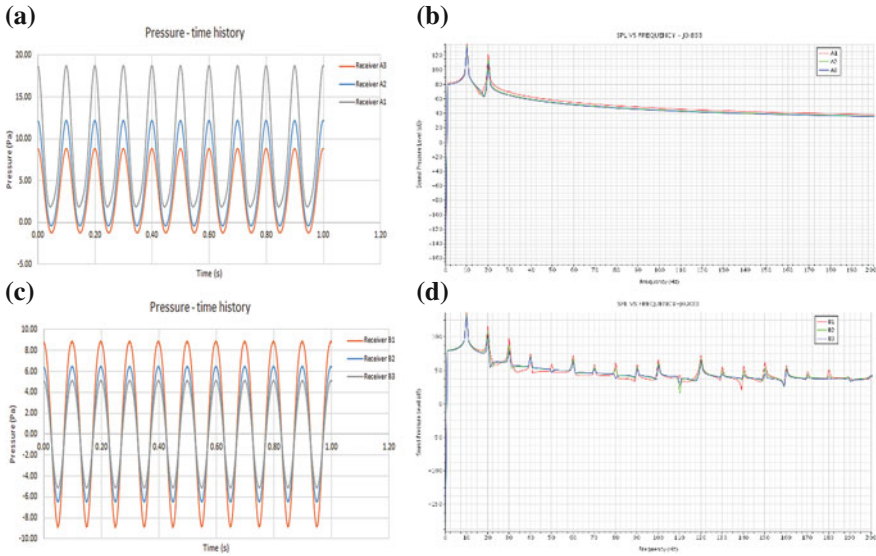


Fig. 7 Pressure-time history and frequency distribution of SPL for $J = 0.833$. **a** Pressure-time history at receiver A1, A2 and A3. **b** SPL at receiver A1, A2 and A3. **c** Pressure-time history at receiver B1, B2 and B3. **d** SPL at receiver B1, B2 and B3

in Fig. 7c where the acoustic pressure reduces as we move from receiver B1 to B3 since the distance from the propeller increases in vertical direction. The SPL versus frequency distribution at receiver B1, B2 and B3 has been obtained using fast Fourier transformation (FFT) of the pressure-time histories predicted at these locations and shown in Fig. 7d. It exhibits two major peaks at 10 and 20 Hz.

5.2 Transient Analysis

Transient analysis was carried out for $J = 0.833$ and a total time of 0.1 s which corresponds to the time taken by the propeller for one complete rotation. The time step was taken as the time required to rotate the propeller by 2° (in accordance with ITTC guidelines for ship self-propulsion using CFD [13]) and corresponds to $5.56e-4$ s. Figure 8 shows that the SPL predicted by MRF, and sliding mesh methods for $J = 0.833$ and $rps = 10$ generally show similar results except at few frequencies.

Comparison of the sound pressure levels predicted by the numerical simulation (using sliding mesh method) with the numerical results of Seol et al. [6] for $J = 0.833$, $rps = 10$ and at a receiver location of 5D is undertaken and is shown in Fig. 9.

Deviations of about 5 dB in the SPL values are seen at frequencies between 12.5 and 25 Hz between the present study and numerical results of Seol et al. [6]. This may possibly be because the analysis by Seol et al. [6] was based on potential-based panel

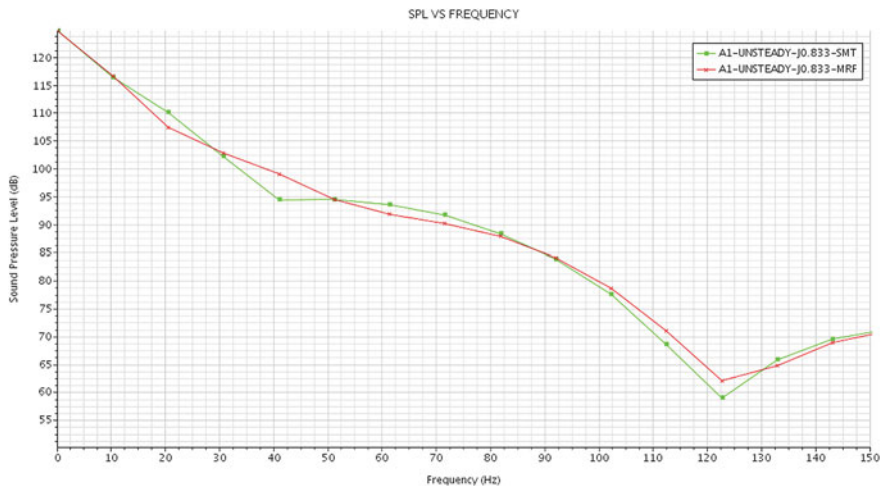


Fig. 8 Comparison of SPL predicted for $J = 0.833$ with MRF and sliding mesh methods

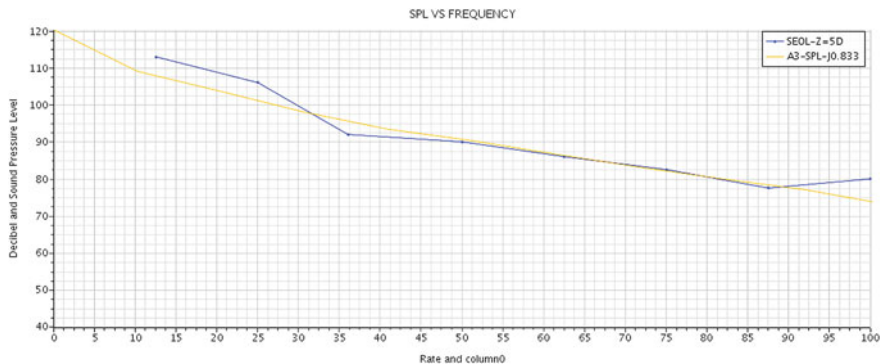


Fig. 9 Comparison of predicted SPL with published numerical results

method coupled with time-domain acoustic analogy to predict the generated noise in non-uniform flow condition, and the present study has been carried out using RANS method for uniform flow condition. Sound pressure levels for $J = 0.2, 0.4, 0.6, 0.8$ and 1.0 at the two receiver locations A1 and B1 using the sliding mesh method are shown in Figs. 10, 11, 12, 13 and 14, respectively.

The SPL obtained at two receiver locations A1 and B1 for different J values up to 500 Hz is shown in Figs. 9, 10, 11, 12 and 13. It is observed that SPL predicted at A1 reduces as advance coefficient increases. This observation is in line with the findings of Mousavi et al. [15] that decreasing the advance coefficients increases the acoustic pressure range of the noise recorded in the receiver.



Fig. 10 SPL at receiver A1 and B1 at $J = 0.2$



Fig. 11 SPL at receiver A1 and B1 at $J = 0.4$



Fig. 12 SPL at receiver A1 and B1 at $J = 0.6$



Fig. 13 SPL at receiver A1 and B1 at $J = 0.8$



Fig. 14 SPL at receiver A1 and B1 at $J = 1.0$

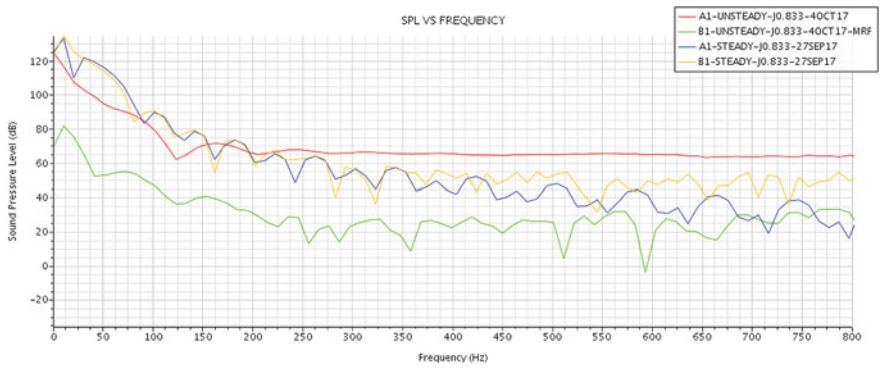


Fig. 15 Comparison of SPL obtained in steady and transient analyses for $J = 0.833$

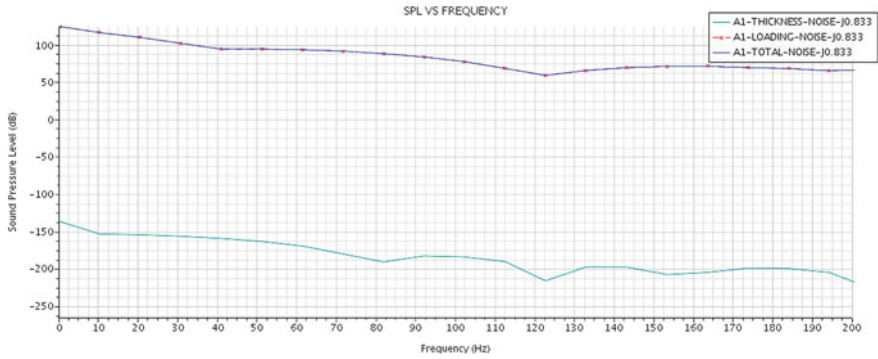


Fig. 16 Comparison of thickness and loading noise at receiver A1

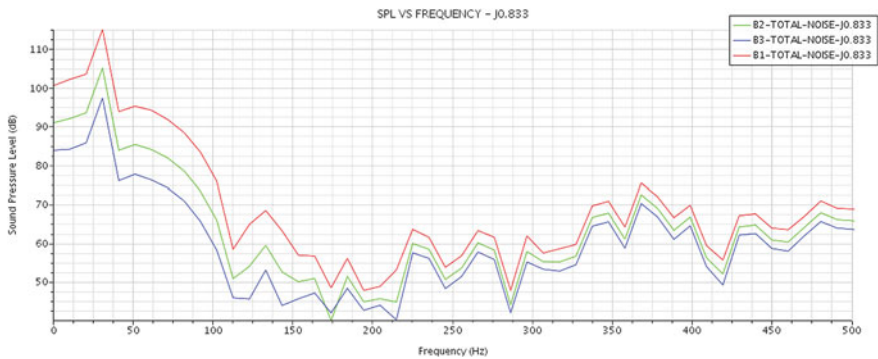


Fig. 17 Comparison of thickness and loading noise at receiver B1

A comparison of the SPL predicted for the steady and transient analyses for $J = 0.833$ is shown in Fig. 15. The study shows that at the receiver location A1, up to 200 Hz, the SPL in the steady state is more than the SPL in transient state and beyond 200 Hz, the SPL in the transient state analysis stabilises to a value of about 70 dB, whereas SPL in the steady-state analysis keeps decreasing. At the receiver location B1, SPL in the transient analysis is always lower than that in the steady-state analysis.

A numerical simulation in order to analyse the contribution of the surface thickness and loading noise to the total surface noise was undertaken for $J = 0.833$. Figure 16 shows the thickness noise and loading noise at receiver A1. It shows that in the far field, the contribution of thickness noise is negligible in comparison to that of loading noise in the downstream direction of the propeller hub. Similar pattern has been seen at receiver locations A2 and A3. Similar observation was also brought out by Jang et al. [16] in 2014 wherein he observed that when the underwater radiated noise for the propeller is predicted in far field, the thickness noise is negligible compared to loading noise even though the advance coefficient is high.

In order to analyse the distribution pattern of loading and thickness noise corresponding to a value of $J = 0.833$, total surface noise components at receiver locations A1 and B1 were analysed. Figure 17 shows the thickness noise and loading noise at receiver B1. From Figs. 16 and 17 and also with the predicted thickness and loading noise values at receiver locations A2, A3, B2 and B3, it is observed that for a $J = 0.833$, loading noise is more dominant in the region on the hub axis (e.g. receiver location A1, A2 or A3) while the thickness noise is more dominant in the plane of blade rotation (e.g. receiver location B1, B2 or B3). This is in line with the acoustic findings of Seol et al. [6] wherein he observed that monopole thickness noise is known to radiate strongest towards the plane of blade rotation and the unsteady dipole loading noise has a strong radiation tendency towards the observer on the hub axis.

6 Conclusions

Numerical analysis to predict the underwater radiated noise of DTMB4119 model propeller operating in the non-cavitating regime in uniform flow (no wake condition) has been undertaken using the CFD code STAR-CCM+; the hydro-acoustic analysis has been undertaken using the FWH equations. The open water hydrodynamic characteristics and the SPL generated by the DTMB4119 model propeller for different advance coefficients have been predicted. Based on the analysis of numerical results, the following conclusions can be drawn:

- The numerical results and experimental data for the open water hydrodynamic characteristics of the model propeller show matching with an error of 2.88% in the open water efficiency at the design J of 0.833.
- The predicted SPL is compared with the numerical results of Seol et al. and shows matching. The deviations in the SPL from the numerical results of Seol et al. may be attributable to the difference in the methodologies adopted in the two studies.
- The SPL decreases as the distance of the observer/receiver from the propeller is increased.
- The moving reference frame and sliding mesh methods of modelling the propeller and its rotation in CFD show almost similar results in terms of SPL at very low rpms (rps = 10 in this study).
- Contribution of the thickness noise is negligible in comparison to that of loading noise at the receiver locations placed on the propeller hub axis for $J = 0.833$.
- Monopole thickness noise radiates strongest towards the plane of blade rotation, and the unsteady dipole loading noise has a strong radiation tendency towards the observer on the hub axis for $J = 0.833$.
- In the future scope of work, we can extend this study to analyse the effect of variation of geometrical parameters like rake angle, skew, section shape on the radiated noise levels of a marine propeller.

References

1. Ross D (2005) Ship sources of ambient noise. *IEEE J Ocean Eng* 30(2):257–261
2. Acoustic measures and sonar principles (2017)
3. Amini H, Steen S (2011) Experimental and theoretical analysis of propeller shaft loads in oblique inflow. *J Sh Res* 55(4):1–21
4. Liu N, Wang S, Guo T, Li X, Yu Z (2011) Experimental research on the double-peak characteristic of underwater radiated noise in the near field on top of a submarine. *J Mar Sci Appl* 10:233–239
5. Elghorab MA, Aly AAE, Elwetedy AS, Kotb MA (2013) Experimental study of non-series marine experimental study of open water non-series marine propeller performance. In: World academy of science, engineering and technology, no. 78, pp 720–726
6. Seol H, Jung B, Suh JC, Lee S (2002) Prediction of non-cavitating underwater propeller noise. *J Sound Vib* 257(1):131–156
7. Seol H, Suh JC, Lee S (2005) Development of hybrid method for the prediction of underwater propeller noise. *J Sound Vib* 288(1–2):345–360
8. Salvatore F, Ianniello S (2003) Preliminary results on acoustic modelling of cavitating propellers. *Comput Mech* 32(4–6):291–300
9. The propulsion committee final report and recommendations to the 22nd ITTC
10. Brizzolara S, Diego V, Gaggero S (2008) A systematic comparison between RANS and panel methods for propeller analysis, Oct
11. Report of propeller committee ITTC 1978
12. ITTC (2014) ITTC—recommended procedures and guidelines—practical guidelines for ship self-propulsion CFD. 7.5-03-03-01 (Revision 00). p 9
13. Kellett P, Turan O, Incecik A (2013) A study of numerical ship underwater noise prediction. *Ocean Eng* 66:113–120
14. Brander P (2015) Calculation results for the 22nd ITTC propulsor committee workshop on propeller RANS/PANEL methods: steady panel method analysis of DTMB 4119 propeller, Jan
15. Mousavi B, Rahrovi A, Kheradmand S (2014) Numerical simulation of tonal and broadband hydrodynamic noises of non-cavitating underwater propeller. *Pol Marit Res* 21(83):46–53
16. Jang JS, Kim HT, Joo WH (2014) Numerical study on non-cavitating noise of marine propeller. *Internoise* 2014:3–8